

Use of the Correlation between Grain Size and Crystallographic Orientation in Crystal Plasticity Simulations

Application to AISI 420 Stainless Steel

Galan Lopez, J.; Hidalgo Garcia, J.

DOI

[10.3390/cryst10090819](https://doi.org/10.3390/cryst10090819)

Publication date

2020

Document Version

Final published version

Published in

Crystals

Citation (APA)

Galan Lopez, J., & Hidalgo Garcia, J. (2020). Use of the Correlation between Grain Size and Crystallographic Orientation in Crystal Plasticity Simulations: Application to AISI 420 Stainless Steel . *Crystals*, 10(9), Article 819. <https://doi.org/10.3390/cryst10090819>

Important note

To cite this publication, please use the final published version (if applicable). Please check the document version above.

Copyright

Other than for strictly personal use, it is not permitted to download, forward or distribute the text or part of it, without the consent of the author(s) and/or copyright holder(s), unless the work is under an open content license such as Creative Commons.

Takedown policy

Please contact us and provide details if you believe this document breaches copyrights. We will remove access to the work immediately and investigate your claim.

Article

Use of the Correlation between Grain Size and Crystallographic Orientation in Crystal Plasticity Simulations: Application to AISI 420 Stainless Steel

Jesús Galán-López *  and Javier Hidalgo *

Department of Materials Science and Engineering, Delft University of Technology, Mekelweg 2, 2628 CD Delft, The Netherlands

* Correspondence: J.GalanLopez@tudelft.nl (J.G.-L.); J.HidalgoGarcia@tudelft.nl (J.H.)

Received: 3 August 2020; Accepted: 14 September 2020; Published: 16 September 2020



Abstract: Crystal plasticity models attempt to reproduce the complex deformation processes of polycrystalline metals based on a virtual representation of the real microstructure. When choosing this representation, a compromise must be made between level of detail at the local level and statistical significance of the aggregate properties, also taking into account the computational cost of each solution. In this work, the correlation between crystallographic orientation and grain size is considered in the definition of virtual microstructures for the simulation of the mechanical behavior of AISI 420 stainless steel (consisting of a ferrite matrix with large carbide precipitates), in order to improve the accuracy of the solution without increasing model complexity or computation time. Both full-field (DAMASK) and mean-field models (Visco Plastic Self Consistent (VPSC)) are used together in combination with experimental results to study the validity of the assumptions done in each of the models.

Keywords: AISI 420; crystal plasticity; representative volume element; VPSC; DAMASK

1. Introduction

The good high temperature properties achievable by martensitic/ferritic steels containing 9–12 wt.% chromium [1–3] will enable an increase in the operating temperatures and pressures of future power plants, resulting in better efficiency and reduction of greenhouse gas emissions. The role of typical M23C6 and MX nitride precipitates on arresting the grain growth and drop in dislocation density during high temperature creep is not fully understood. In particular, coarse M23C6 carbides might cause heterogeneous strains in the ferritic matrix during deformation, creating preferential sites for low angle subgrain development that is believed to impair creep resistance [4]. In order to implement these materials in power plants and other applications, accurate models to describe their plastic behavior are required.

Several physically-based modelling approaches exist, which consider to a greater or lesser extent different microstructural features as the origin of the mechanical response. In particular, crystal plasticity (CP) models take into account the inherent anisotropy of crystals and crystalline aggregates, which is crucial for the prediction of the mechanical behavior of polycrystalline materials. CP models can be categorized in two main groups. Mean-field CP models are deformation models that consider that each grain (defined as a region of material with a distinct crystallographic orientation) is subjected to a homogeneous mechanical state. They include the classical Taylor [5] and Sachs [6] theories—that correspond, respectively, to the upper and lower bounds of the aggregate response—and more complex relaxed constraints models such as ALAMEL [7] and Visco Plastic Self Consistent (VPSC) [8,9] which, at least in principle, better approaches the real behavior. In contrast, in full-field models, a single grain is

spatially resolved by a large number of material points with different mechanical states. Depending on the solver used, current full field models are based on finite element formulations, and are referred to as the Crystal Plasticity Finite Element Method (CPFEM) [10,11], or use fast Fourier transforms in the more recent Crystal Plastic Fast Fourier Transform (CPFPT) models [12,13]. Although full-field models offer a more detailed representation of deformation processes, due to computational limitations they can only simulate a relatively small region of the material, while mean-field models allow the study of the material with greater statistical significance. Mean-field and full-field approaches have been found to be capable of reproducing the mechanical behavior of materials and the evolution of textures upon deformation. However, the prediction of local strain development in chromium steels containing large precipitates and other materials is restricted to the use of full-field models.

In all CP models, information about the material microstructure and the deformation mechanisms at the crystal level needs to be supplied. A synthetic microstructure matching (or partially matching) the stereology and texture of the real material is typically referred to as a Representative Volume Element (RVE). Being able to virtually reconstruct microstructures can be challenging and is the first step to an accurate prediction of the material mechanical behavior. The material microstructure is commonly represented by a discrete set of material grains defined by their crystallographic orientation, cell structure, volume fraction and morphology. The set of grains must be large enough to be representative of the real material but, at the same time, keep a reasonable trade-off with the high computational demands of excessively large synthetic microstructures [14]. Virtual microstructures can be produced based on exact reconstruction methods from an experimentally measured region of the material large enough to ensure statistical homogeneity [15–17]. However, measuring large material microstructure regions in three dimensions—by, for example, electron back-scatter diffraction (EBSD) tomography—is demanding and requires dedicated equipment. Alternatively, a statistically representative volume element can be generated based on the material microstructure statistics [18,19]. Reproducing stereology and texture in the synthetic microstructure is not a trivial task, but different approaches can be found in the literature. The usage of Voronoi tessellations is a popular method for the generation of polycrystalline microstructures, since the nucleation and growth of grains is imitated to some extent by the cell growth process [20,21]. Although the application of multilevel Voronoi tessellations makes it possible to reproduce polycrystals that adhere to complex the distribution of grain size and shape, including the generation of bi-modal microstructures [22,23], a precise synthetic reproduction of the microstructural features of the material is still very challenging [24,25]. For the purposes of this work, the algorithm developed by Groeber et al. [26] proved a reasonable statistical equivalence for most of the relevant morphological and crystallographic parameters of the microstructure. Alternatively, Neper software [22,23] can be used for the generation of complicated microstructures.

Additionally, material properties need to be defined for each phase, including elastic stiffness constants and parameters specific for each deformation mode, such as hardening parameters and strain rate sensitivity. Using appropriate material parameters is as relevant as using a representative set of grains. An optimization algorithm is typically used to find the set of material parameters that best reproduce experimental data. This is a challenging task, since the fitting procedure is also conditioned by the selection of the initial microstructure. The large synthetic microstructures required for high statistical significance often result in simulations too computationally expensive when full-field CP models are employed. Mean-field CP models are computationally more efficient, and therefore less restrictive with the number of grains considered. Although mean-field models cannot reproduce the material behavior at a local level, their averaging capacity makes them ideal to calculate macroscopic behavior when the material is homogenous enough at larger scales. Hence, mean-field CP represents an interesting tool for performing the calibration of material parameters in an efficient manner. The fitted hardening model can then be applied in full-field models to obtain a complete and faithful picture of the material mechanical behavior at different scales.

This work aims to determine an optimal RVE for a chromium steel microstructure consisting of a ferrite matrix with large carbide precipitates. The effect of the size and definition of different virtual microstructures on the simulation of the mechanical behavior of this steel is studied and discussed. A novel method consisting of the correlation between crystallographic orientation and grain size is considered in the definition of virtual microstructures, in order to improve the accuracy of the solution without increasing model complexity or computation time. Both full-field (DAMASK) and mean-field (VPSC) models are used in combination with experimental results to study the validity of the assumptions in each of the models.

2. Materials and Methods

A fully annealed AISI 420 steel rolled sheet with a thickness of 0.45 ± 0.1 mm was used for this study. AISI 420 steel contains 0.32 wt.% C, 0.2 wt.% Si, 0.3 wt.% Mn and 13.7 wt.% Cr as the main alloying elements.

A FEI Quanta 450 scanning electron microscope equipped with a Field Emission Gun (FEG-SEM) and EDAX-TSL, OIM Data Collection software were used to obtain EBSD patterns. The set-up conditions are detailed as: acceleration voltage of 20 kV, spot size #5 corresponding to a beam current of 2.4 nA, working distance of 16 mm, tilt angle of 70° , and a step size of 50 nm in a hexagonal scan grid. The specimen preparation for EBSD consisted of grinding and polishing the specimens with a final polishing step to 0.03 μm colloidal silica solution for 60 min to mitigate the plastic strains introduced at the surface during the process. TSL OIM[®] Analyses 6.0 software was used for post-processing and analysis of the orientation data. A grain confidence index (CI) standardization was applied to the raw data, with a minimum tolerance angle and grain size of 5° and 6 pixels, respectively. It was considered that grains are formed by multiple pixel rows. Thereafter, neighbor-orientation correlation with a tolerance angle of 5° and a minimum confidence index of 0.1 was implemented.

An Instron 5500R electromechanical tensile testing machine was used to generate experimental curves. The experiments were carried out at room temperature, in extension control mode and using a load cell of 50 kN. ASTM E8/E8M–13a standard [27] was followed using a sub-size tensile test specimen geometry. Tensile specimens were machined with the long axis (gauge section) oriented along the sheet rolling direction. The elongation during the tensile test was recorded by a clip-on extensometer with knife-edges, a gauge length of 7.8 mm and a maximum extension of ± 2.5 mm. Uniaxial tension experiments were carried out at strain rates of 0.01 s^{-1} , 0.001 s^{-1} and 0.0001 s^{-1} .

An additional experiment was performed using a miniature flat dog-bone type specimen of $10 \text{ mm} \times 2 \text{ mm} \times 0.45 \text{ mm}$ gauge. The specimen was subjected to tensile elongation of 1.5 mm with a cross-head displacement of 0.005 mm/s in a Deben micromechanical tester. The change in length between the center of two indents placed along the gauge and separated by 1 mm distance was measured to calculate the real plastic strain attained. A square area of approximately $60 \times 50 \mu\text{m}^2$ was delimited by extra indents at which EBSD analysis was conducted in the unstrained condition and after approximately 15% deformation. The same procedure as for microstructure characterization by EBSD was followed before the interrupted test and after making the indents.

3. Modelling

3.1. CPFFT by DAMASK

Full-field crystal plasticity simulations were performed by the spectral solver based on FFT (Fast Fourier Transform) provided by the DAMASK software. Some of the constitutive equations used for the elastic and plastic deformation of synthetic microstructures are broadly presented here. A complete description of the simulation procedure can be found in [12].

The deformation in the continuum theory of crystal plasticity is described as a multiplicative decomposition into reversible and irreversible parts of the deformation gradient F , where the reversible

part F_e accounts for the elastic lattice distortion and rigid rotation, and the irreversible part F_p for the plastic distortion that arises due to slip:

$$F = F_e F_p \quad (1)$$

The stress in the elastic strain regime is expressed in form of the second Piola–Kirchhoff stress tensor S , and depends only on the elastic strain expressed as the Green–Lagrange strain tensor E and the material specific stiffness C , according to:

$$S = C : E \quad (2)$$

$$E = 1/2(F_e F_e^T - 1) \quad (3)$$

For cubic crystals in this study, the elastic stiffness matrix is composed of three independent terms, C_{11} , C_{12} and C_{44} . It is worth to note that reversible dislocation glide, i.e., dislocation anelasticity, is not considered in the model. The evolution of plastic strain is given by:

$$\dot{F}_p = L_p F_p \quad (4)$$

where L_p is the plastic velocity gradient, which can be determined using the shear rates of all slip systems:

$$L_p = \sum_{\beta=1}^N \dot{\gamma}^\eta m_\beta \otimes n_\beta \quad (5)$$

N denotes the number of slip systems. In the present work, twelve slip systems {110}bcc are considered, based on [18,19], while the {211}bcc systems are not taken into account. For the $M_{23}C_6$ carbides, twelve {111}fcc slips systems are considered. m is the slip direction of the slip plane, and n its normal. According with the visco-plastic formulation of Asaro and Needleman [28], the shear rate $\dot{\gamma}^\eta$ on the system η depends on the resolved shear stress, τ^η , and the critical resolved shear stress (CRSS), τ_C^η :

$$\dot{\gamma}^\eta = \dot{\gamma}_0 |\tau^\eta / \tau_C^\eta|^n \text{sign}(\tau^\eta) \quad (6)$$

In the above expression, the exponent n is related to strain rate sensitivity (as further discussed in Section 5), and $\dot{\gamma}_0$ is the reference shear rate. Both parameters are material dependent.

3.2. VPSC90

VPSC90 [8,9] is an implementation of the VPSC model originally developed by Lebensohn and Tomé [8,9]. In the VPSC model, each grain in a polycrystal is considered as an ellipsoidal inclusion in a homogeneous medium with the aggregate properties of the polycrystal. This formalism is solved in VPSC90 using an optimization algorithm based on the gradient descent method. Moreover, VPSC90 takes into account the elastic behavior of the polycrystal and allows the usage of the same pheno-power hardening law used in DAMASK (and further explained in Section 3.3).

If the stress and plastic strain rate in each grain are defined, respectively, by the tensors S_g and \dot{E}_g , then the corresponding polycrystal magnitudes are calculated using a weighted average with respect to the volumetric fraction of each grain (denoted here by w_g). The total strain E in the time increment Δt is obtained adding the elastic strain, calculated using the stiffness tensor C (see the elastic self-consistent method in [8,9]), and the contribution of the plastic strain rate:

$$S = \sum_{g=1}^{Ng} w_g S_g \quad (7)$$

$$\mathbf{E} = \mathbf{C}^{-1} : \mathbf{S} + \Delta t \sum_{g=1}^{N_g} w_g \dot{\mathbf{E}}_g \quad (8)$$

Polycrystal and individual grain magnitudes are also correlated by the interaction equation:

$$\dot{\mathbf{E}}_p - \dot{\mathbf{E}}_g = -\tilde{\mathbf{M}}_g : (\mathbf{S} - \mathbf{S}_g) \quad (9)$$

where $\dot{\mathbf{E}}_p$ is the plastic strain rate of the polycrystal (the multiplier of Δt in Equation (8)) and $\tilde{\mathbf{M}}_g$ is the interaction tensor, which depends on the solution of the viscoplastic Eshelby problem in which grain g is considered an ellipsoidal inclusion in a homogeneous matrix [8,9].

The plastic strain rate of a grain, $\dot{\mathbf{E}}_g$, can be easily calculated as the symmetric part of the symmetric and skew-symmetric decomposition of the velocity gradient, and then the velocity gradient is correlated with the shear induced slip using Equations (5) and (6). The anti-skew symmetric part of the velocity gradient tensor corresponds to a solid rigid rotation which is used to update the orientation of the grain.

3.3. Hardening Law

The widely adopted phenomenological power law is used for the description of slip hardening, both in DAMASK and VPSC simulations. According to this law, the evolution of critical shear stress in the slip plane β , is given by its time derivative $\dot{\tau}_C^\beta$:

$$\dot{\tau}_C^\beta = \sum_{\eta} h_{\beta\eta} \dot{\gamma}^\eta \quad (10)$$

The instantaneous slip-system hardening moduli $h_{\beta\eta}$, in general, depends on the history of slip and provides information about additional hardening caused by interactions of fixed slip systems β and active slip systems η , such that $h_{\beta\eta}$ is determined by:

$$h_{\beta\eta} = q^{\beta\eta} \left[h_0 \left(1 - \tau_C^\eta / \tau_{sat} \right)^a \right] \quad (11)$$

where h_0 , τ_C^η and τ_{sat} are, respectively, the reference hardening, the critical shear stress of plane η , and the saturation shear stress. These parameters depend on the crystal structure and the slip system. The parameter a has not a direct physical meaning but has a direct influence on the development of hardening (typically, $a \geq 1$). The latent hardening parameter, $q^{\beta\eta}$, defines the interaction between system β and η . It is set to one if β and η are coplanar, and to 1.4 otherwise [10].

3.4. Fitting of Parameters

In order to fit the hardening parameters of the model, two procedures were implemented as Python scripts using the VPSC and DAMASK models. Essentially, the methods use experimental data and different optimization algorithms in which successive simulations are run to find the set of parameters that best replicates the material response. The goal in every case is to find the set of hardening parameters for which the difference between the simulated and measured tensile curves is minimised.

A modified Nedler–Mead (NM) simplex algorithm was used for the fitting with DAMASK, following a procedure similar to the one described in [29]. The NM simplex algorithm [30] stands out for its simplicity and easy implementation. Its deterministic character and independence of gradient information make it suitable for the relatively low dimensional optimization inverse problem. The algorithm iteratively adjusts the hardening parameters until the error meets a given tolerance. The bounds of calibrated parameters were defined based on typical values for ferrite [31–34]. The $M_{23}C_6$ carbides are considered to behave as rigid elastic particles, of which elastic constants were obtained by ab-initio calculations in [35].

In the case of the fitting using VPSC, an estimation of the error gradient with respect to the parameters is found and, using this gradient, a new guess of the optimal parameters is made. This process is repeated until the solution converges to an optimal value. More specifically, the minimisation is performed using the Levenberg–Marquardt Algorithm (LMA), that interpolates between the Gauss–Newton algorithm and the method of gradient descent [36].

3.5. Virtual Microstructures

For the DAMASK simulations, different RVEs are generated. Using the Dream 3D software [26,37], two virtual 3D microstructures of different sizes are created, both of them with a grain size distribution and morphology matching the experimental results, as well as the same fraction and size of carbides.

In order to reproduce the experimental ferrite texture and its correlation with grain size with maximum accuracy, crystallographic orientations are assigned independently to the ferrite grains in different size ranges, according to the following procedure:

1. A grain list is generated with the average orientation and area of each ferrite grain in the EBSD experiment (grains are defined with an orientation tolerance of maximum 5°).
2. The list is divided in five bins corresponding to different size ranges, such that each bin contains the same number of grains (approximately 500 grains in the available experimental data). The number of bins was decided such that the number of grains in each bin is enough to reproduce the experimental texture with a low error.
3. For each of these bins, an orientation distribution function (ODF) is calculated using the generalized harmonics series expansion method [38], assuming orthorhombic symmetry.
4. Orientations are randomly assigned to the grains in the RVE according to the ODF calculated for the corresponding grain size range. The orientations are sampled from the discrete texture obtained evaluating the ODF in a regular grid in Euler space, with a spacing of 5°.

Additionally, a third RVE with equal topology to the smaller one is generated, in which crystallographic orientations are directly assigned by the StatsGenerator filter in Dream 3D, based on the EBSD data.

For the VPSC simulations, six different “phases” are considered. Five of them correspond to each of the grain size bins of the ferrite phase calculated as previously explained (step 2), and the sixth one to the carbides. The volumetric fraction of each phase is directly obtained from the grain size distribution, while discrete textures are defined from the list of grains in each size bin. Moreover, an average grain shape is calculated for each of the size bins, and the effect of grain size in hardening behavior is taken into account by modifying the hardening parameters for each ferrite phase according to the Hall–Petch relationship, such that τ_C^η in Equation (11) for the phase with average grain size d takes the value:

$$\tau_C^\eta(d) = \tau_C^\eta(0) + \frac{k_y}{\sqrt{d}} = \tau_C^\eta(d_{avg}) + k_y \left(\frac{1}{\sqrt{d}} - \frac{1}{\sqrt{d_{avg}}} \right) \quad (12)$$

where k_y is the strengthening coefficient, which is fitted together with the hardening parameters, and $\tau_C^\eta(d_{avg})$ is the CRSS value for the average diameter d_{avg} .

4. Results

4.1. Experimental and Virtual Microstructures

The initial microstructure is characterized using two EBSD experiments along different planes obtained through the method explained in Section 2. Inverse pole figure maps, showing averaged grain orientations, are presented in Figure 1. Considering two scans on perpendicular sections allows the derivation of certain aspects of the 3D shape of the grains in a stereological manner without requiring demanding 3D experiments.

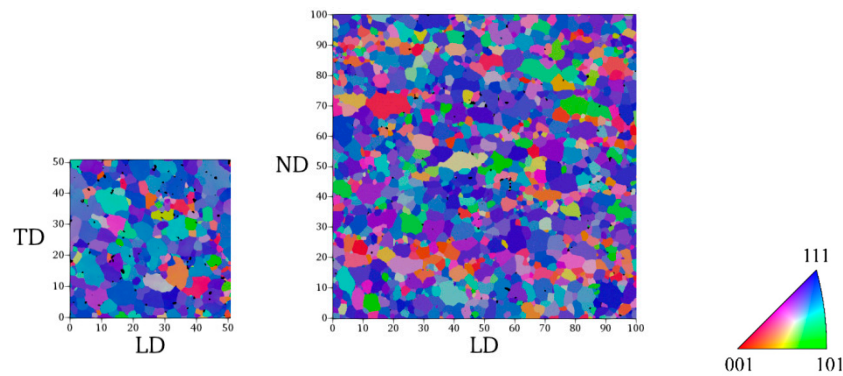


Figure 1. EBSD inverse pole figure (IPF) maps (in the ND direction) along two perpendicular planes: LD–TD on the left, and LD–ND on the right. Carbides are represented in black. Dimensions are given in micrometres.

Equivalent grain diameter, calculated from grain area, and average length of the axis of the equivalent ellipsoid in the rolling direction are calculated combining the results from both measurements. The scan on the LD–TD section is used to calculate the average length of the equivalent ellipsoid axis in the transversal direction, and the experiment along the LD–ND plane is used to calculate the average length of the equivalent ellipsoid axis in the normal direction. In total, 2641 grains and 363 carbides are considered. The diameter and axis length average quantities are always calculated using the geometric average, under the assumption that these magnitudes follow lognormal distributions. Histograms and fitted distributions are shown in Figure 2. It can be seen in the figure that grain diameter and axis lengths indeed follow a distribution which is close to a lognormal function.

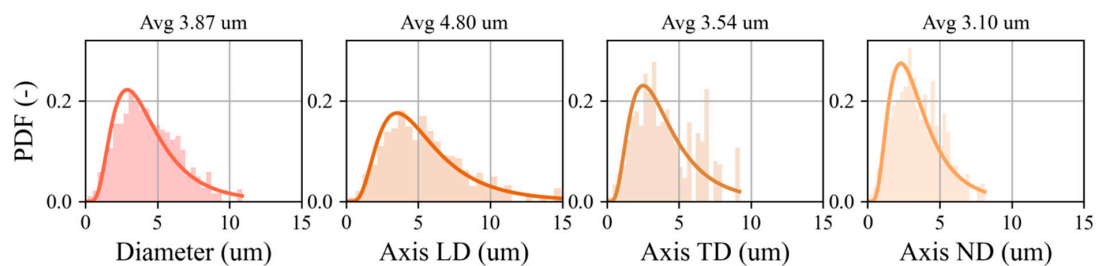


Figure 2. Histograms of grain sizes and equivalent ellipsoid axes and fitted lognormal distributions (continuous lines). On top of each graph, the average value is displayed.

The obtained ODFs for different grain sizes, calculated through the method described in Section 3.5, are shown in Figure 3. The texture of each size bin is displayed in random units with an average value of one so, in order to obtain the probability density for a given orientation and size, it is necessary to multiply by the probability density for the corresponding grain size, which is given in Figure 2. The smallest grains, which represent a small volume fraction, present an almost random texture, with a very weak gamma fibre. The next two bins, which also correspond to relatively small grains and therefore a small volume fraction, show a sharper texture, dominated by the $\{554\}225$ component. As the grain size increases, the texture approaches a stronger and more homogeneous gamma fibre. Since the volume fraction corresponding to this size bin is much higher, this is the predominant texture of the ferrite phase (discussed later).

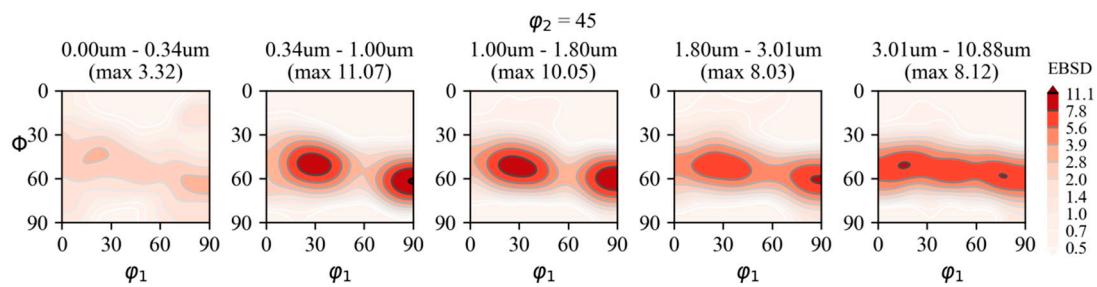


Figure 3. Grain size dependent crystallographic textures. Each $\varphi_2 = 45^\circ$ section corresponds to the ODF calculated for the grains in a different size range (the range for each bin is indicated above the graph, as well as the maximum value of the ODF).

Figure 4 shows three different representative volume elements (RVEs) of the AISI 420 microstructure used in the DAMASK simulations. As explained in Section 3.5, these RVEs are created using Dream 3D, based on the grain size statistics and crystallographic texture collected from the microstructure characterization. $\text{RVE}_{\text{GSODF20}}$ and $\text{RVE}_{\text{ODF20}}$ have a size of $20 \times 20 \times 20$ voxels, with a total of 676 ferrite grains and 178 carbides. Crystallographic orientations are assigned to $\text{RVE}_{\text{GSODF20}}$ extracting discrete textures from the grain size dependent ODFs presented in Figure 3. In the case of $\text{RVE}_{\text{ODF20}}$, the orientations are assigned by the StatsGenerator filter in Dream 3D, using as input the ferrite texture calculated independently of grain sizes. $\text{RVE}_{\text{GSODF50}}$ is generated analogously to $\text{RVE}_{\text{GSODF20}}$, but it has a size of $50 \times 50 \times 50$ voxels, with a total of 3086 ferrite grains and 542 carbides.

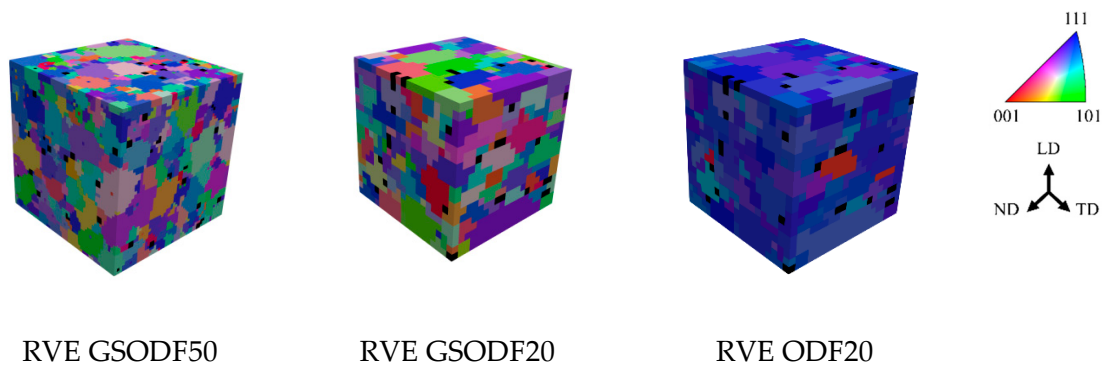


Figure 4. IPF maps in the ND direction of the three generated Representative Volume Elements (RVEs).

The grain size distributions obtained from the generated RVEs are compared with the experimental ones in Figure 5. Since the DAMASK simulations are not dependent on a length scale, it is considered in grain size calculations that the average diameter in the RVE matches the experimental one, so all the RVEs have exactly the same average value as that which was measured. Moreover, the grain sizes in RVE_{50} result in almost the same lognormal distribution as for the EBSD data. For RVE_{20} , there is a larger difference in the standard deviation. A smooth grain size histogram is not reproduced with the reduced number of grains in this RVE.

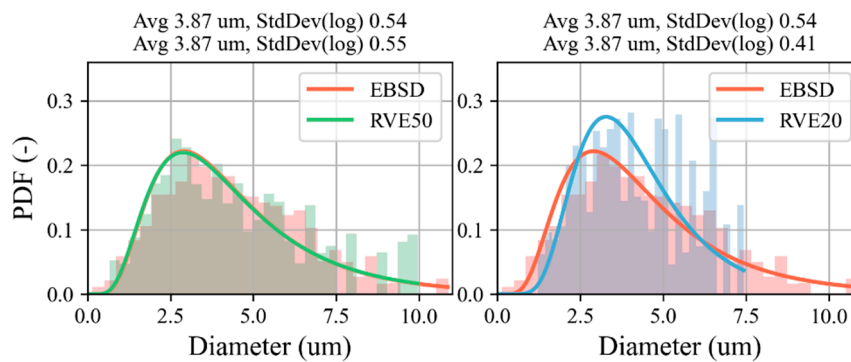


Figure 5. Grain size distribution calculated the RVEs shown in Figure 4 compared with the distribution obtained from the EBSD measurement. The corresponding fitted lognormal distribution is represented with a continuous line.

Crystallographic textures are shown in Figure 6. The experimental ODF, calculated from EBSD data, corresponds to a typical recrystallization texture after cold rolling, with a strong gamma fibre. The difference between the ODF calculated from the different RVEs and the ODF calculated from experimental data, is relatively small (lower than 3.24% and 3.25% for the two GSODF RVEs and 4.17% for RVE_{ODF20}) when compared with the experimental error of the ODF calculated from the EBSD data (3.12%). However, while the textures of the two GSODF RVEs are slightly weaker than the experimental one, the one generated by Dream 3D is much sharper (maximum value of 24.42, compared with 7.89 in the experimental ODF).

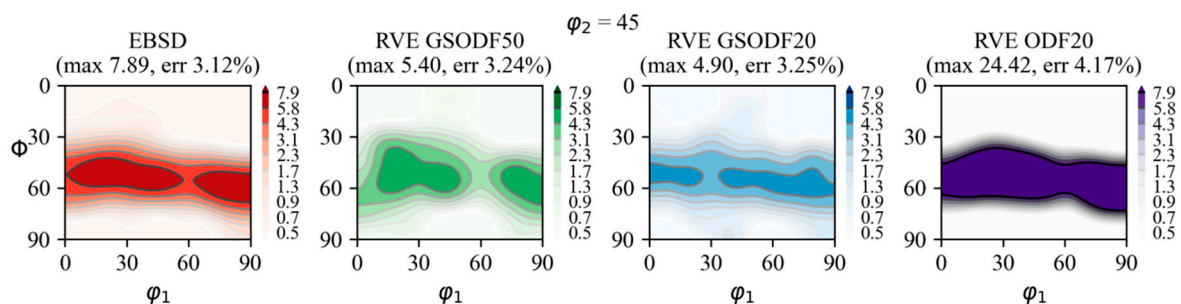


Figure 6. Orientation distribution function ($\varphi_2 = 45^\circ$ section) calculated for the EBSD experiment and the three RVEs shown in Figure 4. The error shown on top indicates the difference between the corresponding discrete texture and the ODF calculated from the EBSD data, or between the calculated ODF and the raw data. And it is calculated as the percentage of variance in intensity for all the points in a discrete grid of 5 degrees in the convenient region of Euler space ($90^\circ \times 90^\circ \times 90^\circ$ for cubic crystal symmetry and orthorhombic sample symmetry).

In Figure 7, grain size dependent crystallographic textures are displayed. These ODFs are obtained applying the same procedure used to calculate the grain size dependent textures of the EBSD measurements (presented in Figure 3), described in Section 3.5. Notice that, due to the different grain size distribution and the binning method used, the size ranges vary between the different microstructures. Both RVE_{GSODF50} and RVE_{GSODF20} present a good correspondence with the experimental textures, with a sharp {554}225 component in smaller grains and a more intense and somewhat more homogeneous gamma fibre for the largest ones. However, RVE_{ODF20} shows a very sharp texture for all grain sizes, always with an intense gamma fibre.

It must be noted that, when the GSODF method is used to assign crystallographic orientations in RVE_{GSODF50} and RVE_{GSODF20}, the textures are reproduced with similar accuracy, although the number of grains in RVE_{GSODF20} is much lower.

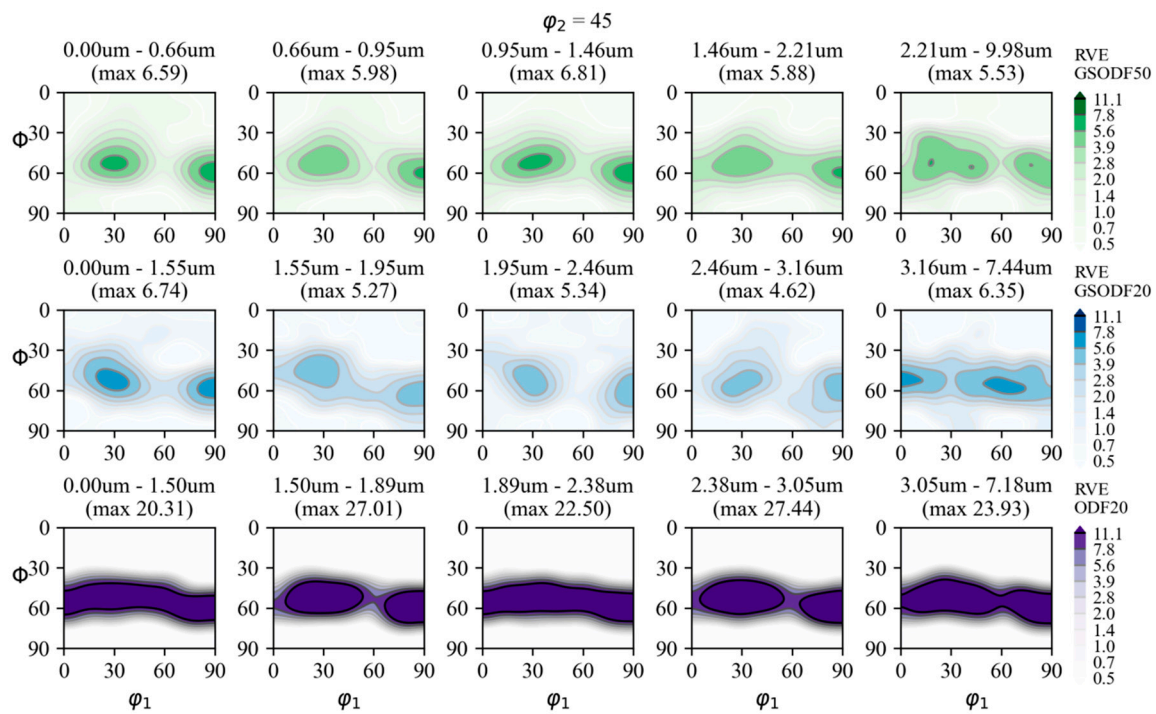


Figure 7. Grain size dependent ODF, calculated for the three RVEs shown in Figure 4. Each $\varphi_2 = 45^\circ$ section corresponds to the ODF calculated for the grains in a different size range.

For the VPSC simulations, the volumetric fraction of each of the five size ranges of ferrite grains is calculated from the grain size distribution in Figure 2. Discrete textures are directly obtained from the list of grains in each size bin of Figure 3 (the original number of ferrite grains is 2641, so approximately 528 grains are used in each ferrite phase). The grain shape is defined differently for each of the ferrite phases, using the axis lengths calculated for each bin presented in Figure 8. The grain size (equivalent diameter) of each ferrite phase is also used in Equation (12) to calculate hardening parameters. The carbide phase is defined with the average shape calculated in the EBSD experiments (ellipsoid axis lengths of 0.78, 0.56 and 0.46 μm).

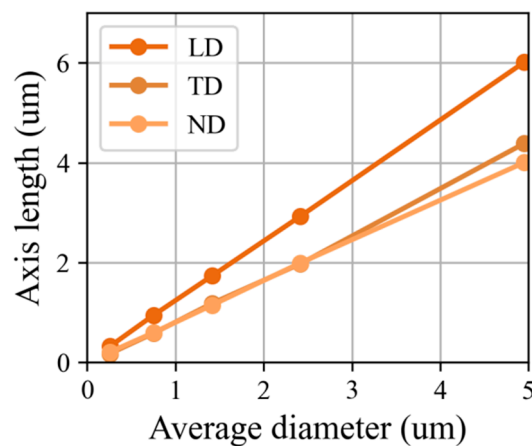


Figure 8. Average length of the equivalent ellipsoid axis for each of the grain size bins into which the EBSD data is divided (see also Figure 2).

4.2. Fitting of Hardening Parameters

Table 1 shows the ferrite and $M_{23}C_6$ carbides materials parameters obtained following the two fitting procedures described in Section 3.4. Relatively similar values of the hardening parameters are obtained using the DAMASK and VPSC models. The most noticeable difference is in the exponent a in expression (11). Simulations showed that the stress partitioned to carbides did not grow to reach values high enough to induce plastic flow, according to the $\tau_{C,0}$ value obtained from the hardness of the $M_{23}C_6$ carbide [39].

Table 1. Adopted and calibrated material parameters for ferrite and $M_{23}C_6$ carbides. The parameters fitted for Visco Plastic Self Consistent (VPSC) correspond to the average grain size ($\tau_c^s(d_{avg})$ in Equation (12)).

Parameter	Unit	Ferrite		$M_{23}C_6$
		VPSC GSODF	DAMASK RVE_{ODF20}	Adopted
C_{11}, C_{12}, C_{44}	GPa	233, 135, 128 [32,33]		472, 216, 135 [35]
$\dot{\gamma}_0$	s^{-1}	1×10^{-6} [32,33]		1×10^{-6}
n_{slip}	-	62.4	65	200
$\tau_{C,0}$	MPa	72.5	77	1200
τ_{sat}	MPa	241.0	226	2000
h_0	MPa	2659.9	2534	20
a	-	2.83	1.75	1.1
k_y	MPa $m^{1/2}$	0.738	-	-

Figure 9 (left) shows the simulated curves obtained using the calibrated parameters with DAMASK and VPSC. Both methods led to a reasonable, good approximation of the observed material behavior in the range of studied strain rates. However, as shown in Figure 9 (right), lower errors with respect to the experimental curve are reached using the VPSC model. At strains above 0.02, the error in the predicted stress always lays below 1%, which is the estimated variance of experimental curves. The divergences with the experimental curve increase at lower strains and none of the two models are able to accurately reproduce the material behavior in the yielding region. This can be consequence, as discussed in [40], of low initial hardening in the AISI 420 steel, due to thermal residual stresses and different population of dislocation defects at grain boundaries, which is not accounted for by any of the models.

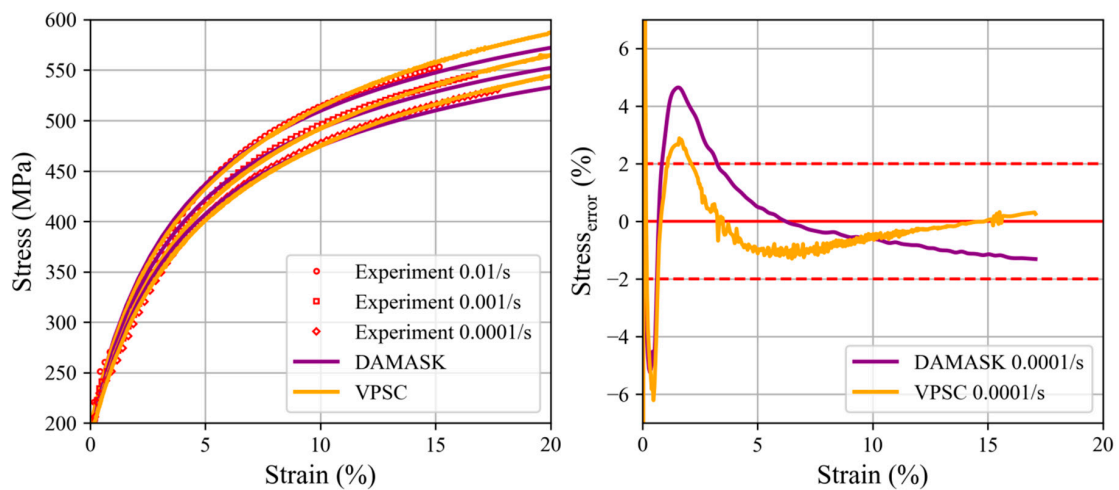


Figure 9. (Left) Experimental tensile test curves at different strain rates compared to simulated curves resulting during the calibration process using VPSC with GSODF full texture and Crystal Plasticity Finite Element Method (CPFEM) with RVE_{ODF20} . (Right) Strain dependence of the error of the predicted stress relative for the 0.0001/s tensile curve (first, cubic spline interpolation was applied for 0 to 0.2 strain and 500 points).

4.3. Deformed Microstructure

After a tensile deformation of 15% is applied to the material as explained in Section 2, new EBSD experiments are performed. In this case, four different scans are performed in different locations of the sample, but on the same LD–ND plane. The obtained IPF maps (in the ND direction) are shown in Figure 10.

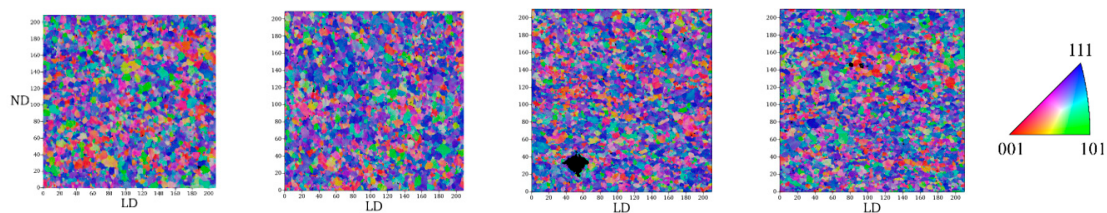


Figure 10. IPF color maps (ND direction) corresponding to the four EBSD measurements performed on the deformed microstructure (uniaxial tension, 15% deformation).

Figure 11 shows the deformed RVEs resulting from DAMASK simulations. The grain size distributions and crystallographic textures corresponding to these RVEs are shown in Figure 12 and are compared with those calculated from the EBSD experiments. The DAMASK simulations are able to capture the change of grain size distribution that takes place during the deformation of the material, as well as reproduce the deformed crystallographic texture. Although in all cases the error with respect to the experimental ODF is lower than 4%, better results are obtained from the GSODF RVEs. It is also observed that the usage of a larger number of points in $RVE_{GSODF50}$ allows a more accurate reproduction of the experimental grain size histogram and crystallographic texture.

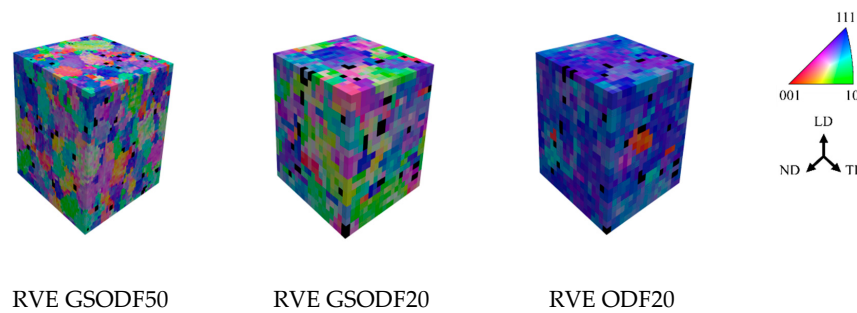


Figure 11. Deformed RVEs after DAMASK simulation under uniaxial tension (deformation: 15%). IPF colors (ND direction), carbides in black.

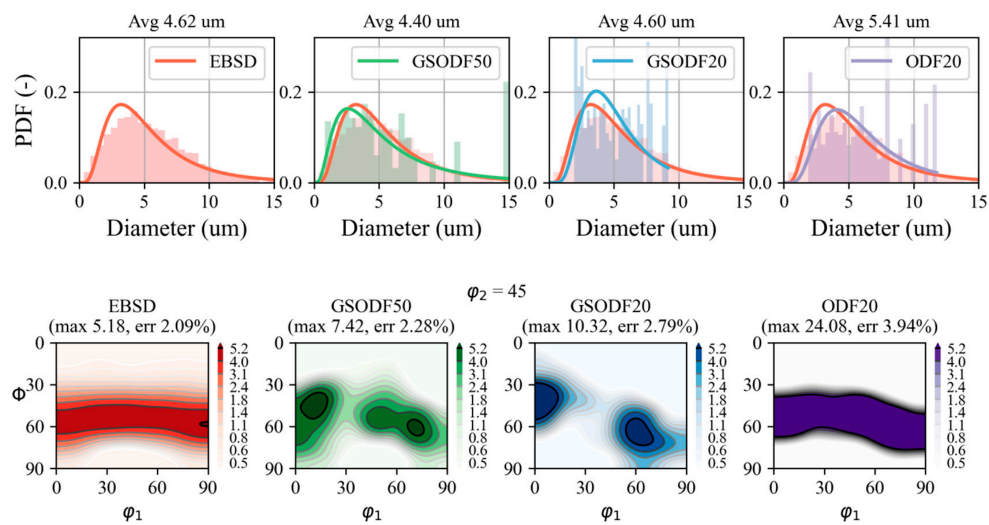


Figure 12. Obtained grain size distributions and crystallographic textures ($\varphi_2 = 45^\circ$ sections) in EBSD experiments and DAMASK simulations. For each grain size distribution, the average grain size is shown on top. On top of the textures, it is shown which is the maximum value and the error with respect to the ODF calculated from the EBSD data, or between the calculated ODF and the raw data (see caption of Figure 6).

The crystallographic textures resulting from the VPSC simulations for each strain rate are shown in Figure 13. In the three simulations, a very similar texture is obtained. Although slightly sharper, these textures are very close to the one calculated from the EBSD measurements (also displayed in the figure). Indeed, the difference between the resulting VPSC textures and the deformed one is almost the same as between the discrete deformed texture and the calculated ODF (2.20% instead of 2.09%).

It is also possible to perform an analysis of the correlation between crystallographic texture and grain size in the deformed microstructure, as the one realized with the initial microstructure in Section 4.1. Figure 14 shows the obtained textures for five different size bins for the EBSD data in Figure 10, the three deformed RVEs in Figure 13, and the VPSC simulation at 0.0001/s in Figure 13. Regarding the EBSD experiments, it is observed that, in contrast with the initial microstructure, the deformed one does not present a strong correlation of crystallographic texture with grain size. Instead, a sharp gamma fibre texture is observed for all size bins, only a bit weaker for the smallest sizes. However, in the simulations, the crystallographic texture shows a clear dependence on grain size. Although the full-field approach used in DAMASK allows the simulation of the grain fragmentation and merging phenomena that take place during the deformation of the material (compare the grain size distributions in Figure 12 with the initial ones presented in Figure 5), grain size dependent textures are not simulated with the same accuracy as the total texture (in Figure 12). In all simulations, a sharper texture is observed for the largest grains, presumably as a consequence of the low number of very

large grains in the generated RVEs. In the case of the VPSC simulation, the sharpness of the textures at different grain sizes after the simulation resembles the initial one (c.f. Figure 3). In the used VPSC model (at difference of, for instance, the model presented in [41]), grains are not fragmented or merged, they can only be reoriented (and deformed), and therefore grain size evolution cannot be simulated, making it impossible to accurately reproduce the grain size dependent textures. Nevertheless, the reorientation of the existing grains produces a noticeable change in the size dependent textures, approaching the strong gamma fibre texture observed in the experiments.

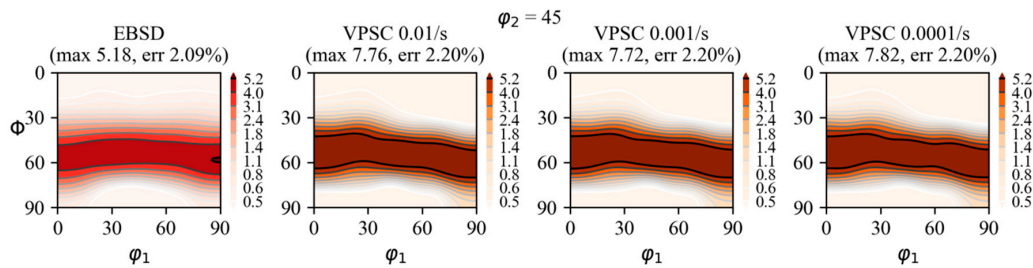


Figure 13. Comparison between deformed texture after uniaxial tension of dog bone specimen deformation 15% at 0.005/s) and DAMASK simulation (deformation: 15% and different strain rates), using parameters fitted with RVE 20 ODF.

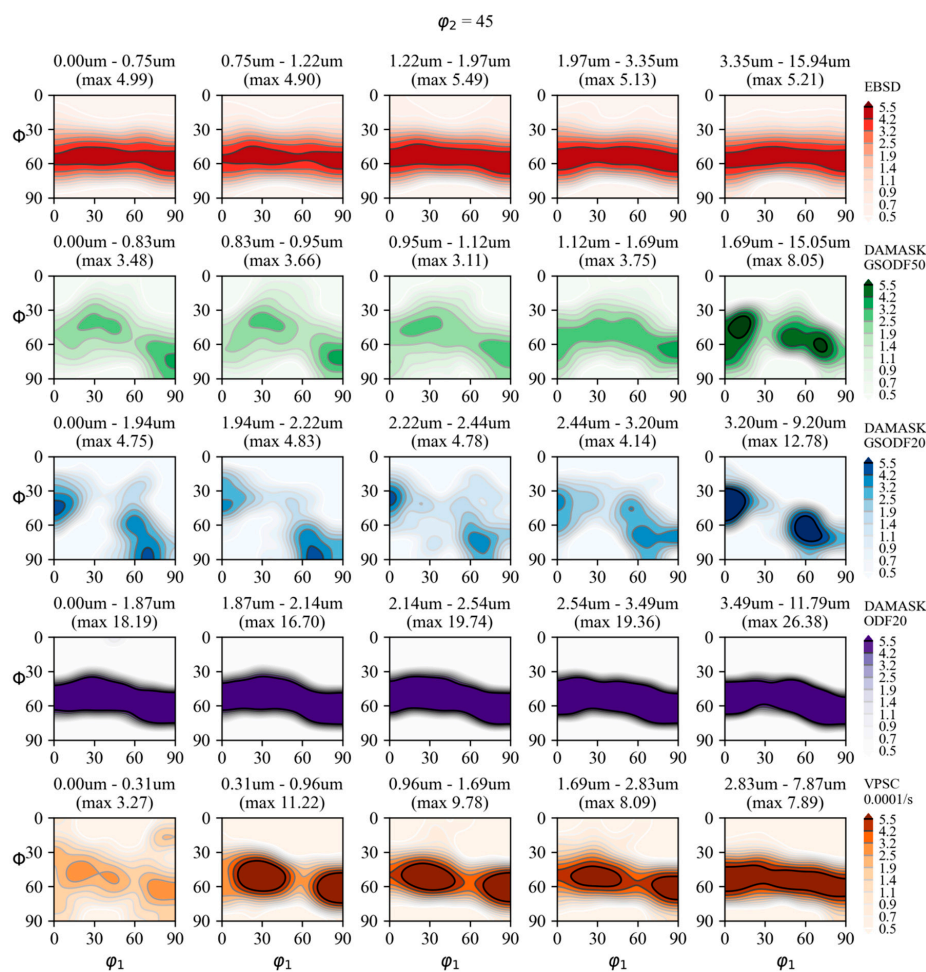


Figure 14. Grain size dependent ODFs (deformation: 15%) obtained from the EBSD measurements, the DAMASK simulations with the GSODF50, GSODF20 and ODF20 RVEs, and the VPSC simulation at a strain rate of 0.0001/s.

5. Discussion

Both DAMASK and VPSC approaches arrive at a relatively similar set of calibrated parameters for ferrite, as shown in Table 1. According to the adopted hardening law, plastic flow begins only when favourable oriented slip systems are activated. This is controlled in a single crystal by $\tau_{C,0}$, which is considered to account for all the strengthening mechanisms, such as the presence of grain boundaries, dislocations, or small precipitates, which affect the material yielding. An estimation of $\tau_{C,0}$ in the polycrystal can be made by connecting this parameter with the yield stress (σ_y) and the arithmetic mean of the Taylor factor, M , using the expression:

$$\sigma_y = M\tau_{C,0} \quad (13)$$

A yield stress of 222 MPa was measured by the 0.2% offset method at 0.0001 s^{-1} strain rate. Considering that the Taylor factor M for the ferrite in present steel is 2.9, and applying Equation (13), a value of 76.5 MPa is obtained for $\tau_{C,0}$, which is close to the respective parameters calibrated using DAMASK and VPSC (c.f. Table 1). It is worth noting that former calculation translates the local CRSS to the yield stress using a simple “averaged” Taylor factor, which is equivalent to applying the full constraint Taylor model. This is a very basic model, but it can provide an accurate initial guess of the boundaries of $\tau_{C,0}$.

The strain rate sensitivity parameter (exponent n in Equation (11)) can be deduced directly from the comparison of the tensile curves at different strains rates [42]. Considering that the virtual-work principle $\tau d\gamma = \sigma d\varepsilon$ applies [43], then:

$$\dot{\varepsilon} = \dot{\varepsilon}_0 \left(\frac{\sigma(\dot{\varepsilon})}{\sigma(\dot{\varepsilon}_0)} \right)^n \Rightarrow \frac{\sigma(\dot{\varepsilon})}{\sigma(\dot{\varepsilon}_0)} = \left(\frac{\dot{\varepsilon}}{\dot{\varepsilon}_0} \right)^{1/n} \quad (14)$$

Applying Equation (14) to the experimental tensile data, under the assumption that quasi-static conditions are fulfilled at a strain rate of $\dot{\varepsilon}_0 = 0.0001/\text{s}$, the value $n = 65$ is obtained. Figure 15 shows how the experimental results compare with this value, as well as the curves corresponding to different n values. The value $n = 65$ is used for the DAMASK simulations at different strain rates. The value fitted using VPSC, 62.4, is very close to the experimental result and, as Figure 15 shows, will produce a similar strain rate dependence of tensile behavior.

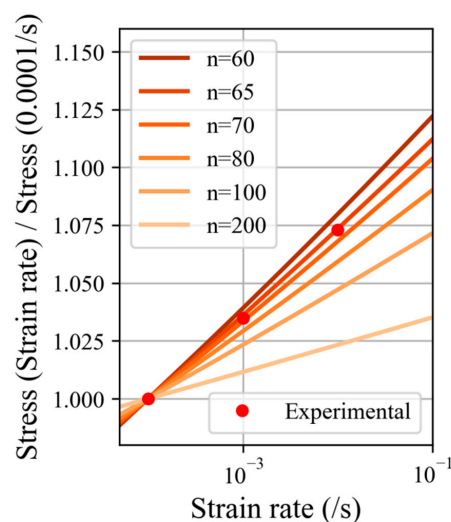


Figure 15. Strain rate dependence of stress for different values of the strain rate sensitivity exponent. The squares represent the strain rate dependence of the material extracted from the three tensile curves at different strain rates in Figure 9, assuming that $\dot{\varepsilon}_0 = 0.0001/\text{s}$.

Although both DAMASK and VPSC can be successfully used for the fitting of the hardening parameters, the method that uses the VPSC model has the advantage of requiring much less computational resources. Indeed, while the fitting process using the DAMASK model needed more than 12 h, using eight processors, to find the optimal values for a single strain rate, the method using VPSC allows the performance of the optimization in approximately 2 h for the three strain rates considered (only one processor is used for each simulation, so the three simulations at different strain rates can be run in parallel). These differences in running times are even more significant when it is taken into account that, since the used optimization algorithms can only find local minima, it is necessary to repeat the process several times with different initial parameters. It is therefore desirable to be able to fit the hardening parameters always using the faster VPSC method. In order to evaluate this possibility, the DAMASK simulations are repeated using the parameters fitted with the VPSC model. For completeness, the VPSC simulations are also repeated using the parameters fitted with DAMASK.

Figure 16 shows the tensile curves simulated with the DAMASK and VPSC models using the parameters obtained with the two calibration methods, as well as the simulated transversal and normal strains. As shown in Figure 9, both fitting methods accurately represent the experimental results. However, clear differences are observed when the fitted parameters are applied to simulations with different models and RVEs. It is remarkable that, when the parameters fitted using VPSC are applied to the RVEs used with DAMASK, a better approximation is obtained with more detailed RVEs. A relatively good match is obtained with $RVE_{GSODF50}$, followed by $RVE_{GSODF20}$ and, finally, RVE_{ODF20} . However, when the parameters fitted using DAMASK and RVE_{ODF20} are employed, the next RVE with the best match is $RVE_{GSODF20}$, although the original microstructure is better reproduced by $RVE_{GSODF50}$, with five times more grains. A similar trend is observed in the graphs of strain in the transversal and normal directions (also shown in Figure 16). $RVE_{GSODF50}$ and VPSC yield similar results, while $RVE_{GSODF20}$ is slightly different, and RVE_{ODF20} shows a completely different behavior.

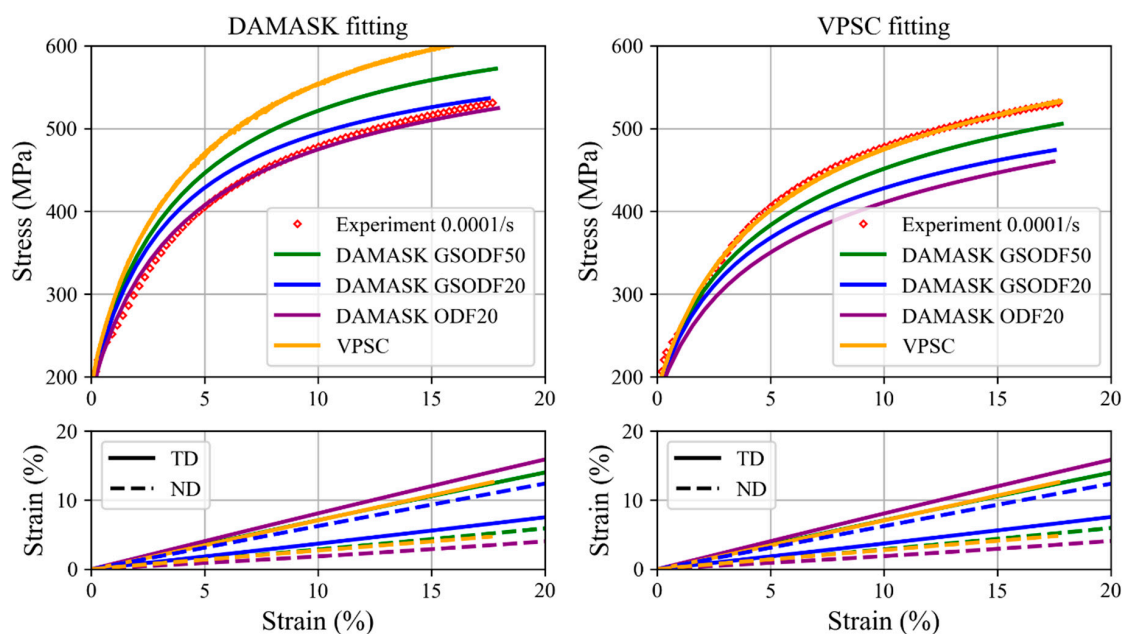


Figure 16. Experimental and simulated tensile test curves and simulated transversal and normal strain resulting from: application of material parameters set obtained after calibration with VPSC and GSODF full texture (at left); and application of material parameter set obtained after calibration with CPFEM and RVE_{ODF20} (at right).

To sum up, it appears that the use of the VPSC model to fit hardening parameters for DAMASK does not present any inconvenience that is not present when a small RVE is directly used in DAMASK.

On the contrary, it approaches the response obtained from highly detailed RVEs, supposedly closer to the real behavior of the material.

Similar conclusions can be extracted from the grain size distributions and crystallographic textures, presented in Figure 17 (c.f. Figure 12). The grain size distributions and crystallographic textures obtained with RVE_{GSODF50} and RVE_{GSODF20} and the parameters fitted using VPSC are practically the same as when using the parameters fitted using RVE_{ODF20}. Surprisingly, the experimental grain size distribution and crystallographic texture are better reproduced in the RVE_{ODF20} simulations that use the parameters fitted with VPSC than in those performed with the parameters obtained with DAMASK using the same RVE. Therefore, it is clear that VPSC in combination with the grain size dependent textures approach is an effective method for obtaining an adequate set of materials parameters: mechanical behavior is better correlated with the quality of the RVE used in the simulation, experimental microstructural evolution is reproduced with higher accuracy, and the time and computational resources required to perform the fitting are much lower.

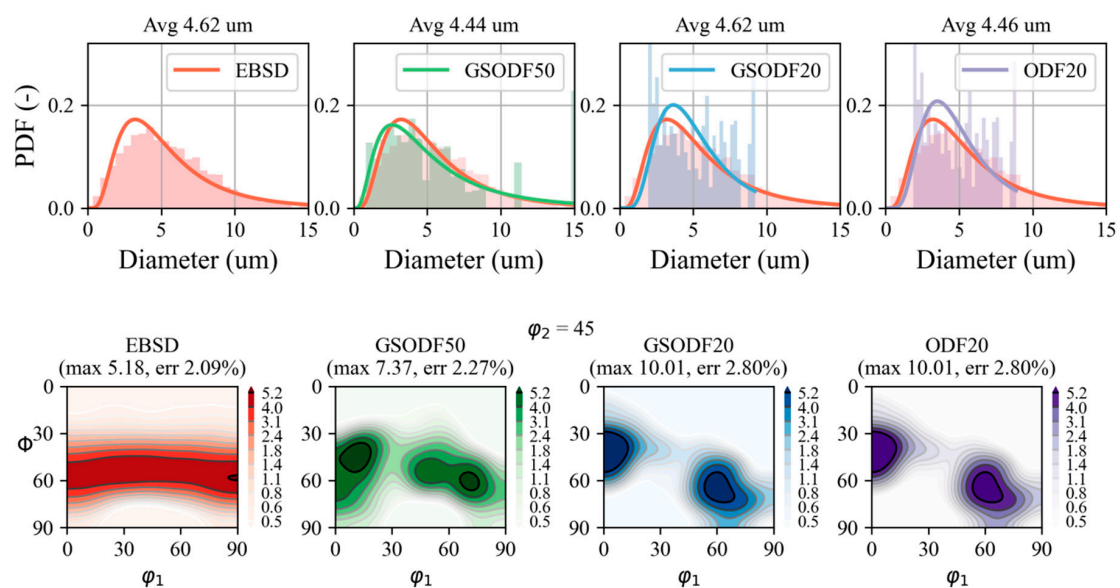


Figure 17. Obtained grain size distributions and crystallographic textures ($\phi_2 = 45^\circ$ sections) in EBSD experiments and DAMASK simulations using the model parameters fitted with VPSC. For each grain size distribution, the average grain size is shown on top. On top of the textures, it is shown which is the maximum value and the error with respect to the ODF calculated from the EBSD data, or between the calculated ODF and the raw data (see caption of Figure 6).

6. Conclusions

Both the DAMASK and VPSC crystal plasticity models can be used to perform simulations of the mechanical behavior and microstructural evolution of AISI420 steel. However, how the real microstructure of the material is represented in the model and plays a fundamental role in the outcome of the simulations. In this work, the correlation between grain size and crystallographic texture has been applied in mean-field and full-field crystal plasticity simulations, after the analysis of EBSD data showed that there is a sharpening of the crystallographic texture for grains of larger size. The use of this correlation enables a more truthful description of the real microstructure, and the additional data makes it possible to perform a deeper analysis of the results.

In the VPSC simulations, grain shape, crystallographic texture and hardening law are defined dependent on grain size. Using a homogenization model like VPSC allows the consideration of a virtual microstructure representative enough from a statistical point of view and with enough efficiency to be used for the fitting of material parameters. The obtained model is further applied in full-field DAMASK simulations, where the correlation between grain size and crystallographic texture is introduced by

assigning the orientations of the RVE grains depending on their size. The simulations are capable of reasonably reproducing the correlations observed in the deformed microstructure.

Author Contributions: J.G.-L. and J.H. equally contributed to conceptualisation, design of methodology, formal analysis and in the writing—original draft preparation, review and editing. J.G.-L. focused on the VPSC90 simulations and in the implementation of GSODF concept into representative volume elements. J.H. focused on the simulations with DAMASK software and performed and analyzed the experimental results. All authors have read and agreed to the published version of the manuscript.

Funding: This research has received funding from the European Union’s Research Fund for Coal and Steel (RFCS) research program under grant agreement RFCS-2015-709418 (MuSTMeF) and from the VMAP—ITEA 16010 project via the ITEA 3 cluster of the European research initiative EUREKA.

Acknowledgments: The authors want to acknowledge L. Kestens and J. Sietsma for their wise comments and R. Petrov and F. Verduyck for performing the EBSD experiments.

Conflicts of Interest: The authors declare no conflict of interest.

References

1. Masuyama, F. History of power plants and progress in heat resistant steels. *ISIJ Int.* **2001**, *41*, 612–625. [[CrossRef](#)]
2. Rojas, D.; Garcia, J.; Prat, O.; Sauthoff, G.; Kaysser-Pyzalla, A.R. 9%Cr heat resistant steels: Alloy design, microstructure evolution and creep response at 650 °C. *Mater. Sci. Eng. A* **2011**, *528*, 5164–5176. [[CrossRef](#)]
3. Vivas, J.; Capdevila, C.; Altstadt, E.; Houska, M.; San-Martín, D. Importance of austenitization temperature and ausforming on creep strength in 9Cr ferritic/martensitic steel. *Scr. Mater.* **2018**, *153*, 14–18. [[CrossRef](#)]
4. Vivas, J.; Capdevila, C.; Altstadt, E.; Houska, M.; Sabirov, I.; San-Martín, D. Microstructural Degradation and Creep Fracture Behavior of Conventionally and Thermomechanically Treated 9% Chromium Heat Resistant Steel. *Met. Mater. Int.* **2019**, *25*, 343–352. [[CrossRef](#)]
5. Taylor, G.I. Plastic strain in metals. *Plast. Strain Met.* **1938**, *62*, 307–324.
6. Sachs, G. Plasticity problems in metals. *Trans. Faraday Soc.* **1928**, *24*, 84–92. [[CrossRef](#)]
7. Houtte, P.V.; Li, S.; Seefeldt, M.; Delannay, L. Deformation texture prediction: From the Taylor model to the advanced Lamel model. *Int. J. Plast.* **2005**, *21*, 589–624.
8. Lebensohn, R.A.; Tomé, C.N. A self-consistent anisotropic approach for the simulation of plastic deformation and texture development of polycrystals: Application to zirconium alloys. *Acta Metall. Mater.* **1993**, *41*, 2611–2624. [[CrossRef](#)]
9. Galán, J.; Verleysen, P.; Lebensohn, R.A. An improved algorithm for the polycrystal viscoplastic self-consistent model and its integration with implicit finite element schemes. *Model. Simul. Mater. Sci. Eng.* **2014**, *22*, 55023. [[CrossRef](#)]
10. Roters, F.; Eisenlohr, P.; Hantcherli, L.; Tjahjanto, D.D.; Bieler, T.R.; Raabe, D. Overview of constitutive laws, kinematics, homogenization and multiscale methods in crystal plasticity finite-element modeling: Theory, experiments, applications. *Acta Mater.* **2010**, *58*, 1152–1211. [[CrossRef](#)]
11. Roters, F.; Eisenlohr, P.; Bieler, T.; Raabe, D. *Crystal Plasticity Finite Element Methods: In Materials Science and Engineering*; John Wiley & Sons: Hoboken, NJ, USA, 2010. [[CrossRef](#)]
12. Roters, F.; Diehl, M.; Shantraj, P.; Eisenlohr, P.; Reuber, C.; Wong, S.L.; Maiti, T.; Ebrahimi, A.; Hochrainer, T.; Fabritius, H.O.; et al. DAMASK—The Düsseldorf Advanced Material Simulation Kit for modeling multi-physics crystal plasticity, thermal, and damage phenomena from the single crystal up to the component scale. *Comput. Mater. Sci.* **2019**, *158*, 420–478. [[CrossRef](#)]
13. Eisenlohr, P.; Diehl, M.; Lebensohn, R.A.; Roters, F. A spectral method solution to crystal elasto-viscoplasticity at finite strains. *Int. J. Plast.* **2013**, *46*, 37–53. [[CrossRef](#)]
14. Chatterjee, K.; Echlin, M.P.; Kasemer, M.; Callahan, P.G.; Pollock, T.M.; Dawson, P. Prediction of tensile stiffness and strength of Ti-6Al-4V using instantiated volume elements and crystal plasticity. *Acta Mater.* **2018**, *157*, 21–32. [[CrossRef](#)]
15. Zaeferrer, S.; Wright, S.I.; Raabe, D. Three-Dimensional Orientation Microscopy in a Focused Ion Beam—Scanning Electron Microscope: A New Dimension of Microstructure Characterization. *Metall. Mater. Trans. A* **2008**, *39*, 374–389. [[CrossRef](#)]

16. Balzani, D.; Scheunemann, L.; Brands, D.; Schröder, J. Construction of two- and three-dimensional statistically similar RVEs for coupled micro-macro simulations. *Comput. Mech.* **2014**, *54*, 1269–1284. [[CrossRef](#)]
17. Pirgazi, H. On the alignment of 3D EBSD data collected by serial sectioning technique. *Mater. Charact.* **2019**, *152*, 223–229. [[CrossRef](#)]
18. Swaminathan, S.; Ghosh, S.; Pagano, N.J. Statistically equivalent representative volume elements for unidirectional composite microstructures: Part I—Without damage. *J. Compos. Mater.* **2006**, *40*, 583–604. [[CrossRef](#)]
19. Brands, D.; Balzani, D.; Scheunemann, L.; Schröder, J.; Richter, H.; Raabe, D. Computational modeling of dual-phase steels based on representative three-dimensional microstructures obtained from EBSD data. *Arch. Appl. Mech.* **2016**, *86*, 575–598. [[CrossRef](#)]
20. Zhang, P.; Balint, D.; Lin, J. Controlled Poisson Voronoi tessellation for virtual grain structure generation: A statistical evaluation. *Philos. Mag.* **2011**, *91*, 4555–4573. [[CrossRef](#)]
21. Bargmann, S.; Klusemann, B.; Markmann, J.; Schnabel, J.E.; Schneider, K.; Soyarslan, C.; Wilmers, J. Generation of 3D representative volume elements for heterogeneous materials: A review. *Prog. Mater. Sci.* **2018**, *96*, 322–384. [[CrossRef](#)]
22. Quey, R.; Dawson, P.R.; Barbe, F. Large-scale 3D random polycrystals for the finite element method: Generation, meshing and remeshing. *Comput. Methods Appl. Mech. Eng.* **2011**, *200*, 1729–1745. [[CrossRef](#)]
23. Kasemer, M.; Quey, R.; Dawson, P. The influence of mechanical constraints introduced by β annealed microstructures on the yield strength and ductility of Ti-6Al-4V. *J. Mech. Phys. Solids* **2017**, *103*, 179–198. [[CrossRef](#)]
24. Vittoriotti, M.; Kok, P.J.J.; Sietsma, J.; Jongbloed, G. Accurate representation of the distributions of the 3D Poisson-Voronoi typical cell geometrical features. *Comput. Mater. Sci.* **2019**, *166*, 111–118. [[CrossRef](#)]
25. Vittoriotti, M.; Kok, P.J.J.; Sietsma, J.; Li, W.; Jongbloed, G. General framework for testing Poisson-Voronoi assumption for real microstructures. *Appl. Stoch. Models Bus. Ind.* **2020**. [[CrossRef](#)]
26. Groeber, M.; Ghosh, S.; Uchic, M.D.; Dimiduk, D.M. A framework for automated analysis and simulation of 3D polycrystalline microstructures. Part 2: Synthetic structure generation. *Acta Mater.* **2008**, *56*, 1274–1287. [[CrossRef](#)]
27. ASTM-E8-E8M-13a. *Standard Test Methods for Tension Testing of Metallic Materials*; ASTM International: West Conshohocken, PA, USA, 2013; Volume E8 E8M-13a, p. 28.
28. Asaro, R.J.; Needleman, A. Overview no. 42 Texture development and strain hardening in rate dependent polycrystals. *Acta Metall.* **1985**, *33*, 923–953. [[CrossRef](#)]
29. Chakraborty, A.; Eisenlohr, P. Evaluation of an inverse methodology for estimating constitutive parameters in face-centered cubic materials from single crystal indentations. *Eur. J. Mech. A/Solids* **2017**, *66*, 114–124. [[CrossRef](#)]
30. Nelder, J.A.; Mead, R. A Simplex Method for Function Minimization. *Comput. J.* **1965**, *7*, 308–313. [[CrossRef](#)]
31. Yalcinkaya, T.; Brekelmans, W.A.M.; Geers, M.G.D. BCC single crystal plasticity modeling and its experimental identification. *Model. Simul. Mater. Sci. Eng.* **2008**, *16*, 85007. [[CrossRef](#)]
32. Tasan, C.C.; Hoefnagels, J.P.M.; Diehl, M.; Yan, D.; Roters, F.; Raabe, D. Strain localization and damage in dual phase steels investigated by coupled in-situ deformation experiments and crystal plasticity simulations. *Int. J. Plast.* **2014**, *63*, 198–210. [[CrossRef](#)]
33. Maresca, F.; Kouznetsova, V.G.; Geers, M.G.D. On the role of interlath retained austenite in the deformation of lath martensite. *Model. Simul. Mater. Sci. Eng.* **2014**, *22*, 45011. [[CrossRef](#)]
34. Maresca, F.; Kouznetsova, V.G.; Geers, M.G.D. Reduced crystal plasticity for materials with constrained slip activity. *Mech. Mater.* **2016**, *92*, 198–210. [[CrossRef](#)]
35. Liu, Y.; Jiang, Y.; Xing, J.; Zhou, R.; Feng, J. Mechanical properties and electronic structures of M₂₃C₆ (M = Fe, Cr, Mn)-type multicomponent carbides. *J. Alloy. Compd.* **2015**, *648*, 874–880. [[CrossRef](#)]
36. Press, W.H.; Flannery, B.P.; Teukolsky, S.A.; Vetterling, W.T. *Numerical Recipes in C: The Art of Scientific Computing*; Cambridge University Press: Cambridge, UK, 1988.
37. Groeber, M.A.; Jackson, M.A. DREAM.3D: A Digital Representation Environment for the Analysis of Microstructure in 3D. *Integr. Mater. Manuf. Innov.* **2014**, *3*, 56–72. [[CrossRef](#)]
38. Van Houtte, P. A method for the generation of various ghost correction algorithms—The example of the positivity method and the exponential method. *Texture Stress Microstruct.* **1991**, *13*, 199–212. [[CrossRef](#)]

39. Inoue, A.; Arakawa, S.; Masumoto, T. Effect of Alloying Elements on Defect Structure and Hardness of M23C6 Type Carbides. *Trans. Jpn. Inst. Met.* **1979**, *20*, 585–592. [[CrossRef](#)]
40. Hidalgo, J.; Vittoriotti, M.; Farahani, H.; Vercruyse, F.; Petrov, R.; Sietsma, J. Influence of M23C6 Carbides on the Heterogeneous Strain Development in Annealed 420 Stainless Steel. Available online: <https://ssrn.com/abstract=3558254> (accessed on 15 September 2020).
41. Zecevic, M.; Lebensohn, R.A.; McCabe, R.J.; Knezevic, M. Modeling of intragranular misorientation and grain fragmentation in polycrystalline materials using the viscoplastic self-consistent formulation. *Int. J. Plast.* **2018**, *109*, 193–211. [[CrossRef](#)]
42. Galán-López, J.; Verleysen, P. Simulation of the plastic response of Ti–6Al–4V thin sheet under different loading conditions using the viscoplastic self-consistent model. *Mater. Sci. Eng. A* **2018**, *712*, 1–11. [[CrossRef](#)]
43. Przybyła, C.; Adams, B.; Miles, M. Methodology for Determining the Variance of the Taylor Factor: Application in Fe-3%Si. *J. Eng. Mater. Technol.* **2007**, *129*. [[CrossRef](#)]



© 2020 by the authors. Licensee MDPI, Basel, Switzerland. This article is an open access article distributed under the terms and conditions of the Creative Commons Attribution (CC BY) license (<http://creativecommons.org/licenses/by/4.0/>).